BIOCHEMISTRY
including biophysical chemistry & molecular biology

Article

pubs.acs.org/biochemistry

Primary and Secondary Photodynamics of the Violet/Orange Dual-Cysteine NpF2164g3 Cyanobacteriochrome Domain from *Nostoc punctiforme*

Sean M. Gottlieb,[†,§] Peter W. Kim,[†,§] Scott C. Corley,[†,§] Dorte Madsen,[†] Samuel J. Hanke,[†] Che-Wei Chang,[†] Nathan C. Rockwell,[‡] Shelley S. Martin,[‡] J. Clark Lagarias,[‡] and Delmar S. Larsen*[,†]

[†]Department of Chemistry and [‡]Department of Molecular and Cell Biology, University of California—Davis, One Shields Avenue, Davis, California 95616, United States

Supporting Information

ABSTRACT: Cyanobacteriochromes (CBCRs) are cyanobacterial photoreceptors distantly related to phytochromes. Like phytochromes, CBCRs photointerconvert between two photostates that accompany photoisomerization of their bilin chromophores. While phytochromes typically exhibit red/far-red photocycles, CBCR photocycles are much more diverse, spanning the near-ultraviolet and the entire visible region. All CBCRs described to date have a conserved Cys residue covalently attached to the linear tetrapyrrole (bilin) chromophore; two CBCR subfamilies also exploit a second thioether linkage to the chromophore for detection of near-ultraviolet to blue light. Here, we present the photodynamic analysis of the insert-Cys CBCR NpF2164g3, a representative of the second class of two-cysteine CBCRs. Using broadband transient absorption pump−probe spectroscopy, we characterize the primary (100 fs to 10 ns) and secondary (10 ns to 1 ms) photodynamics in both directions, examining photodynamics over nine decades of time. Primary isomerization dynamics occur on a ∼10 ps time scale for both forward and reverse reactions. In contrast to previous studies on Tlr0924, a representative of the other class of two-cysteine CBCRs, formation and elimination of the second linkage are slower than the 1 ms experimental range probed here. These results extend our understanding of dual-cysteine CBCR photocycles in the phytochrome superfamily.

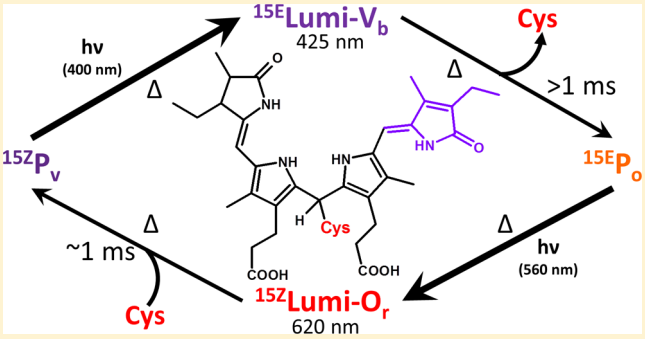

Phytochromes are photosensory proteins first discovered as regulators of plant development.[1] Phytochromes typically adopt a red-absorbing P_r state in darkness, and absorption of red (660 nm) light triggers conversion to a far-red-absorbing state that can be converted back via absorption of far-red (730 nm) light. In this red/far-red photocycle, the covalently attached linear tetrapyrrole (bilin) chromophore undergoes photoisomerization about the 15,16-double bond on the ultrafast time scale to generate primary Lumi-R and Lumi-FR photoproducts, respectively.[2−5] Subsequent steps on the nanosecond to millisecond time scales take place on the electronic ground-state surface to eventually generate a stable or metastable P_{fr} state. Cyanobacteriochromes (CBCRs) are recently discovered cyanobacterial photosensors distantly related to phytochromes that display similar photochromic switching activity. Although phytochrome photocycles are typically limited to the red/far-red region, CBCR photocycles range from the ultraviolet to the near-infrared.[3,6−9] Multiple CBCR subfamilies have been resolved to date, displaying varied spectral and dynamic responses, but all exhibit 15,16-double-bond primary photoisomerization as is seen in phytochromes.[3,10,11] CBCRs also share a conserved Cys residue with plant and cyanobacterial phytochromes that forms a covalent thioether linkage to the C3 ethylidene side chains of bilins such as phycocyanobilin (PCB) or phytochromobilin.

Two short-wavelength-absorbing CBCR families have conserved second Cys residues: the DXCF subfamily[9,12−14] and the insert-Cys subfamily.[6] In both subfamilies, the conserved second Cys forms a covalent linkage to the C10 atom of the bilin chromophore (Figure 1A) to create two separate violet-to-blue-absorbing π-conjugated systems.[6,9,10,13] Photoexcitation of dual-cysteine linked, dark-adapted states triggers isomerization of the bilin's 15,16-double bond from the *Z* configuration to the *E* configuration, flipping the D-ring within the chromophore binding pocket and, in many cases, leading to thermal elimination of the second linkage on the electronic ground-state surface.[6,9,10,13] Excitation of the *15E* chromophore triggers isomerization to the *15Z* configuration, which, in many cases, is followed by thermal reformation of the second linkage to complete the two-Cys photocycle (Figure 1B).[6,9,10,13] The shortening of the conjugated π system by the second linkage shifts the absorption spectrum to much shorter

Received: November 19, 2013
Revised: January 10, 2014
Published: January 18, 2014

   dx.doi.org/10.1021/bi4015538 | *Biochemistry* 2014, 53, 1029−1040

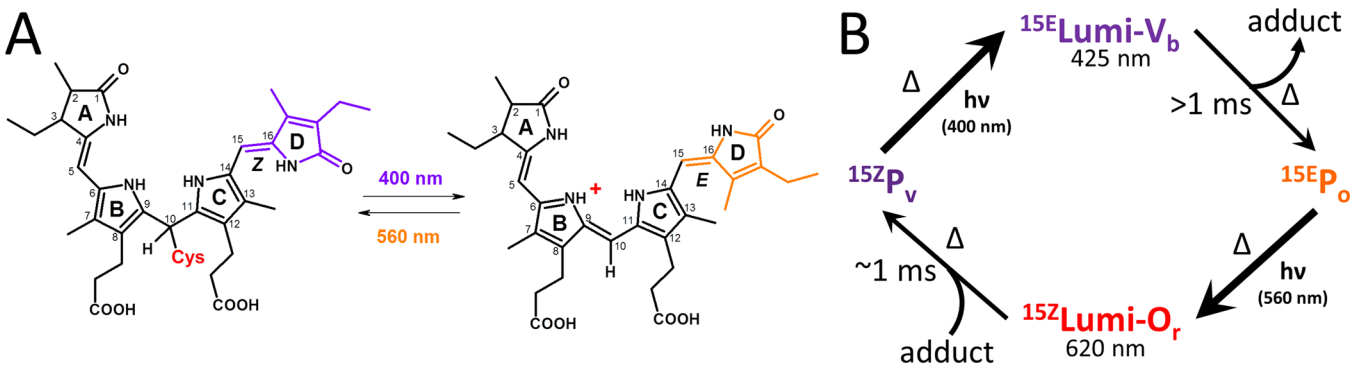

Figure 1. (A) Changes in chromophore structure during the violet/orange photocycle of NpF2164g3. (B) Simplified four-state, four-reaction scheme for the NpF2164g3 photocycle (only isomerization, adduction formation/breaking, and primary photointermediates are shown). The first cysteine linkage of the protein to the A-ring of the PCB chromophore is not shown.

wavelengths, conferring peak absorption in the near-UV to blue.

In the DXCF subfamily, the second Cys residue is part of a loosely conserved Asp-Xaa-Cys-Phe (DXCF) motif.[7,9,10,14,15] Some DXCF CBCRs can autocatalytically isomerize the bound PCB chromophore into phycoviolobilin (PVB). Because both bilins have identical C- and D-rings, their doubly linked blue-absorbing states are nearly identical.[9,12,13] However, after photoconversion and linkage cleavage, DXCF CBCRs with PVB absorb at considerably shorter wavelengths than their PCB-bound counterparts.[8,9,12,13,15] The diversity and versatility of this subfamily has been revealed through characterization of many of these photosensors.[9,10,15−18] DXCF CBCRs include the first CBCR to be characterized in vitro (SyPixJ[19]), the only two-Cys CBCR yet described on an ultrafast time scale (Tlr0924[20]), and the only CBCR for which there is structural information for both photostates (TePixJ[21,22]).

The insert-Cys family of two-Cys CBCRs places the second cysteine in a nonconserved, extended insertion loop.[6] As insert-Cys CBCRs are not closely related to DXCF CBCRs, evolution of the second linkage has occurred more than once in CBCRs.[6] No structures are yet available for the insert-Cys subfamily, but backbone assignments of the *15E* photoproduct state of one example, NpF2164g3 from *Nostoc punctiforme*, show that the regions around both Cys residues are unstructured.[23] This adaptation may facilitate location of the second Cys in close proximity to the chromophore. Known insert-Cys CBCRs do not form PVB, but elimination of the second linkage upon photoconversion is variable. Thus, known insert-Cys photocycles include violet/orange and UV/blue.[6] In NpF2164g3, elimination upon photoconversion does occur, resulting in a violet/orange photocycle with $^{15Z}P_v$ and $^{15E}P_o$ photostates (Figure 1A).

The mechanisms underlying the spectral responses of CBCR domains are a topic of ongoing investigations. Primary photochemistry is thought to be the same as in phytochromes, which is supported for many CBCRs by a static denaturation assay.[8,9,11,13,15,17,24] To date, picosecond dynamics have been reported only for the red/green CBCRs NpR6012g4 and NpF2164g6 from *N. punctiforme*[25−28] and for the DXCF CBCR Tlr0924 from *Thermosynechococcus elongatus*.[20] Secondary (nanosecond to millisecond) data have been presented only for two red/green CBCRs, NpR6012g4 and AnPixJ from *Nostoc* sp. PCC 7120.[29−31] The DXCF subfamily of dual-cysteine CBCRs have been more extensively studied than the insert-Cys CBCRs. NpF2163g3 thus serves as a valuable model system for the insert-Cys subfamily, which has garnered much interest recently including both structural and photochemical studies.[6,15,23]

Here, we present the first photodynamic study for an insert-Cys CBCR. We have characterized both primary (100 fs to 10 ns) and secondary (10 ns to 10 ms) photodynamics for NpF2164g3 in both the forward ($^{15Z}P_v \rightarrow {}^{15E}P_o$) and reverse ($^{15E}P_o \rightarrow {}^{15Z}P_v$) reactions using pump−probe transient absorption (TA) spectroscopy with broadband detection. The forward photodynamics of NpF2164g3 exhibit some similarity to those of the DXCF CBCR Tlr0924, but differ from those resolved for red/green CBCR domains. Despite their independent evolution, our studies suggest that there may be common aspects to all two-Cys CBCR photocycles.

MATERIALS AND METHODS

Sample Preparation. NpF2164g3 was prepared as previously described.[6] Static absorption spectra were acquired at 25 °C on a Cary 50 modified to allow top-down illumination of the sample to initiate photochemistry[32] using bandpass filters at 400 ± 35 and 600 ± 20 nm.

Transient Signals. The ultrafast primary (100 fs to ∼8 ns) dynamics of both the forward and reverse reactions were measured as discussed previously,[33] and more details can be found in the Supporting Information. The excitation wavelengths used for initiating the forward (400 nm) and reverse (565 nm) primary signals were selected to be near the peaks of the static absorption spectra (Figure S1). The instrument response function for both directions was estimated at ∼100 fs from the signal rise times of the excited-state absorption (ESA) bands.

The instrumental setup for measuring the secondary dynamics is based on a similar design to the apparatus used to characterize the primary dynamics, with the broadband probe pulses generated by focusing a portion (∼1 μJ) of the 800 nm Ti:Sapphire amplified laser (Spectra-Physics, Spitfire Pro) into a slowly translating 10 mm thick CaF_2 crystal. The probe pulses were imaged via a spectrograph (Oriel Instruments 77480) onto a 512 pixel silicon diode array (Hamamatsu C7884-8L003). The key difference between the primary and secondary experimental setups is that the excitation pulses for initiating the secondary signals originate from a separate independent Q-switched diode-pumped solid-state YAG laser (Pulselas-A-532-300). For the secondary forward reaction dynamics, 355 nm excitation pulses (Figure S1) were generated by the third harmonic generation of the YAG's 1064 nm

dx.doi.org/10.1021/bi4015538 | *Biochemistry* 2014, 53, 1029−1040

fundamental light via a 5 mm thick potassium dihydrogen phosphate crystal. For the secondary reverse reaction dynamics, 525 nm excitation pulses were used from the second harmonic output of the laser (Figure S2). The instrument response functions for the secondary signals in both directions were estimated at ~500 ps on the basis of the signal rise times of the data. Under the conditions of the experiment, the data collected up to ~1 ms are unaffected by the flow conditions and repetition laser excitation (500 kHz).

The 1 ms transient spectra were collected from the 1 kHz pulse train by shifting the probe pulse slightly before (~1 ps) the pump pulse, which results in the collection of a transient spectrum initiated by the pump pulse from 1 ms before. To facilitate this further, the sample flow rate is typically slowed so that incomplete refreshing of new sample occurs within the excitation laser volume in the flow cell. Under normal flow conditions, this pre-time-zero signal (1 ms spectrum) is negligible. Subsequent harmonic dynamics (e.g., 4 ms) are not a major factor in these spectra because the flow rate has completely refreshed (within the excitation volume) on this time scale.

RESULTS

The ground-state absorption spectra of NpF2164g3 in the $^{15Z}P_v$ and $^{15E}P_o$ (no adduct) states are contrasted in Figure 2.[6]

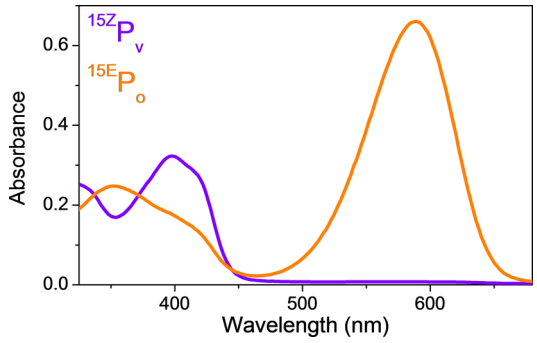

Figure 2. Static ground-state absorption spectra are shown for the $^{15Z}P_v$ dark ground state (violet curve) and in the $^{15E}P_o$ ground state (orange curve). Spectra are scaled to the peak absorption at 280 nm (not shown). Spectra of the excitation pulses used for the resolved dynamics are shown in Figure S1.

Although the $^{15E}P_o$ state photoreaction can be excited with orange light without generating contaminating $^{15Z}P_v$ signals, the exclusive generation of $^{15Z}P_v$ signals is difficult because of the strong spectral overlap between the low-energy transition of $^{15Z}P_v$ and the higher-energy Soret band of $^{15E}P_o$. This overlap prevents complete photochemical formation of $^{15Z}P_o$;[23] hence, weak $^{15E}P_o$ signal contamination was observed in the $^{15Z}P_v$ signals discussed below. This contamination was removed by subtracting a small (~5%) amount of P_o signals from the data.

Primary Forward Photodynamics ($^{15Z}P_v \rightarrow {}^{15E}$Lumi-$V_b$). Transient spectra at selected times are presented in Figure 3A. The early spectra (<10 ps) exhibit two broad and slightly overlapping positive bands from 425 to 700 nm (black and red curves) that are attributed to the excited-state absorption (ESA) of $^{15Z}P_v$*. The trough at 500 nm is likely the result of an overlapping negative stimulated emission (SE) band; such a band was observed in the excited-state $^{15Z}P_b$* spectrum of Tlr0924.[20] Whereas signals at shorter wavelengths exhibit more complex behavior (Figure 3B,C), multiexponential ESA decay

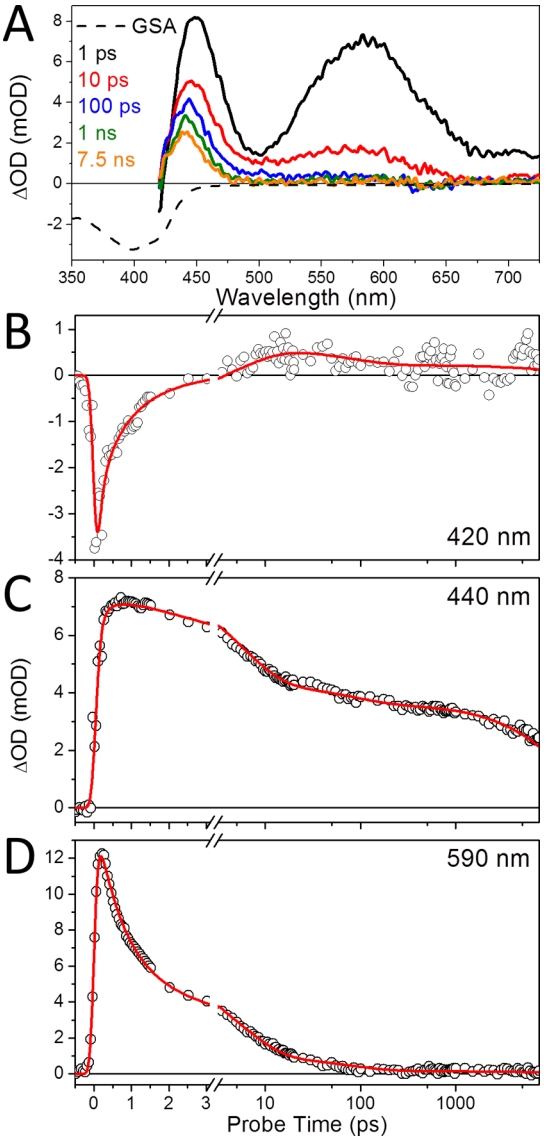

Figure 3. Ultrafast (<8 ns) transient signals of the forward reaction ($P_v \rightarrow P_o$) dynamics. (A) Transient spectra at selected probe times overlaid with the inverted $^{15Z}P_v$ dark-adapted ground state (dashed curves). (B–D) Kinetic traces (black circles) at the indicated wavelengths are shown overlapping the global fits (red curves) from the target model described in Figure 9.

kinetics can be cleanly tracked at 590 nm ESA, leading to zero signal at longer times (Figure 3D). Decay of $^{15Z}P_v$* is followed by a population with nonzero absorption at 440 nm (Figure 3B,C); this population persists beyond the experimental window (Figure 3C) but is resolvable at long times (see below). Further evidence for such a population can be seen at 420 nm (Figure 3B), a wavelength corresponding to the edge of the negative ground-state bleach (GSB) of $^{15Z}P_v$. At 420 nm, initial negative GSB is replaced by a positive signal at ca. 10 ps, and this positive population then decays slowly. We therefore assign the positive signals in the vicinity of 450 nm to the initial $^{15Z}P_v$* ESA followed by the formation and subsequent decay of the isomerized, blue-absorbing ^{15E}Lumi-V_b primary photoproduct.

Secondary Forward Photodynamics (^{15E}Lumi-$V_b \rightarrow {}^{15E}P_o$). We follow the subsequent evolution of ^{15E}Lumi-V_b at later times, but we were limited to excitation at 355 nm in this

dx.doi.org/10.1021/bi4015538 | Biochemistry 2014, 53, 1029–1040

time regime, resulting in a much lower signal-to-noise ratio in the measured TA signals (Figure 4). This was due, in part, to

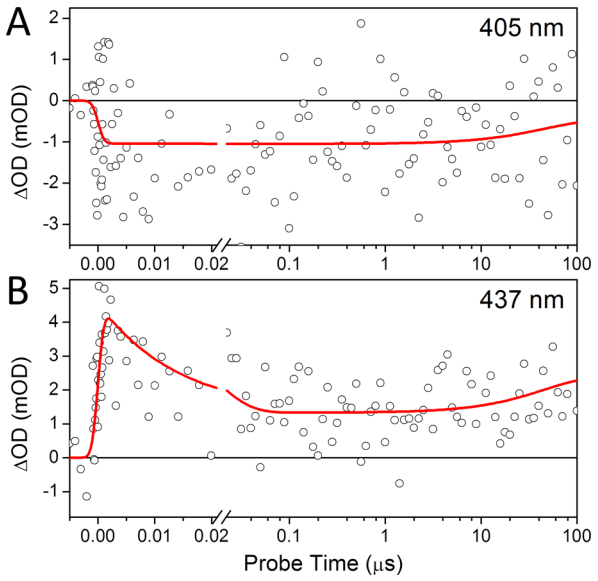

Figure 4. Secondary (>100 μs) kinetics of the forward dynamics ($P_v \rightarrow P_o$) at select wavelengths (as indicated). Fit from global analysis from the EADS analysis in Figure 10 are shown (solid red curves).

rapid photodegradation of the sample from the high-energy 355 nm excitation photons. Nevertheless, we were able to observe a clear trend that was better resolved in the global analysis (Figure 4, red curves; see below). Whereas the GSB exhibits little evolution at 405 nm on the 100 μs time scale (Figure 4A), the decay of ^{15E}Lumi-V_b observed in the ultrafast signals at 440 nm is clearly observed at 437 nm (Figures 3C and 4B). We also observed subsequent growth at 437 nm on a 45 μs time scale. No red-shifted intermediates were observed within the 100 μs delay window, indicating that adduct breakage occurs on a slower time scale (data not shown).

Primary Reverse Photodynamics ($^{15E}P_o \rightarrow {}^{15Z}$Lumi-$O_r$). For the reverse reaction, ultrafast TA spectra at selected times are presented in Figure 5A. Excitation of $^{15E}P_o$ at 565 nm generated a well-resolved GSB band peaking near 580 nm with two flanking ESA bands spanning 425−525 and 650−750 nm. No clearly resolved SE band was observed, although such a band could be masked by overlapping ESA bands. Spectra at later times exhibit a new positive absorption peaking near 630 nm that is assigned to the primary ^{15Z}Lumi-O_r photoproduct.

Evolution of $^{15E}P_o$* into ^{15Z}Lumi-O_r was clearly observed in the kinetic traces (Figure 5B−D). At 470 nm, slow ESA decay is seen without competing signals (Figure 5B). This ESA decay is correlated with GSB decay (575 nm: Figure 5C) and with ^{15Z}Lumi-O_r growth (635 nm: Figure 5D). As with the forward primary photoproduct ^{15E}Lumi-V_b (Figure 3C), partial decay of ^{15Z}Lumi-O_r was seen on a 10 ns time scale (Figure 5D). This slower decay of photoproduct also correlated with an apparent decay of the GSB (Figure 5C). However, it is unclear from the ultrafast data alone whether ^{15Z}Lumi-O_r decays directly into the GSB (commonly assumed and implying loss of photoproduct) or instead evolves into a secondary intermediate with an absorption that strongly overlaps the GSB. We examined the secondary dynamics of the reverse reaction to address this uncertainty.

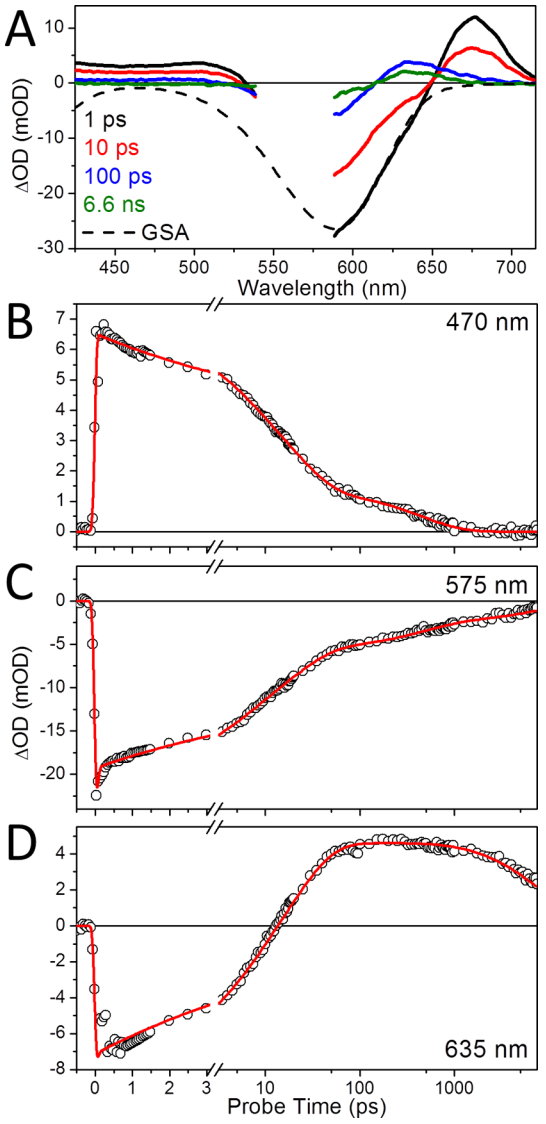

Figure 5. Primary (<8 ns) transient signals of the reverse reaction ($P_o \rightarrow P_v$). (A) Transient spectra at select probe times indicated in the legend overlaid with the inverted $^{15E}P_O$ ground state (dashed curve). (B−D) Kinetic traces (black circles) at the indicated wavelengths with fits (red curves) from the target model described in Figure 11.

Secondary Reverse Photodynamics (^{15E}Lumi-$O_r \rightarrow {}^{15Z}P_v$). Secondary TA spectra for the reverse reaction were obtained with a good signal-to-noise ratio using excitation at 532 nm (Figure 2) and exhibited complex spectral evolution (Figures 6 and 7). The ESA decay kinetics are notably slower than in the ultrafast experiment (1.3 ns and 460 ps, respectively), which could indicate an excitation-wavelength dependence in NpF2164g3, as discussed below. The ^{15Z}Lumi-O_r decay observed at late times in the ultrafast kinetics (Figure 5D) is well-resolved in the secondary dynamics (Figures 6A and 7B), with concomitant growth of broad absorption between 500 and 575 nm (Figure 6). The absorption of this Meta-O_g intermediate strongly overlaps the GSB. Therefore, its growth resembles the decrease of GSB, resolving the ambiguity of the ultrafast signals at late times.

Meta-O_g evolves between 60 ns and 2 μs (Figure 6B), with an apparent regrowth of the negative GSB band and formation of a positive absorption spanning 625−675 nm. This Meta-O_r

dx.doi.org/10.1021/bi4015538 | Biochemistry 2014, 53, 1029−1040

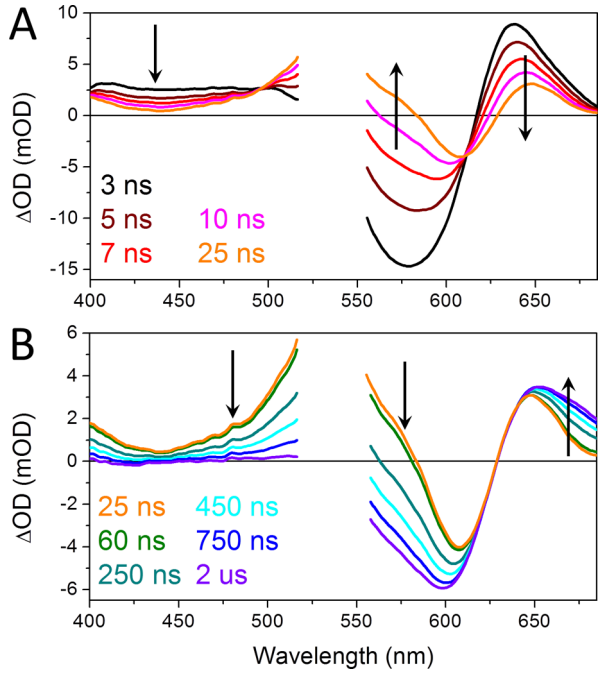

Figure 6. Secondary (<1 μs) transient spectra of the reverse reaction ($P_o \rightarrow P_v$) initiated by 532 nm excitation (A) from 3 to 25 ns and (B) from 60 ns to 2 μs. The 25 ns spectrum (orange curves) appears in both panels for visual aid. Arrows indicate evolution of spectra.

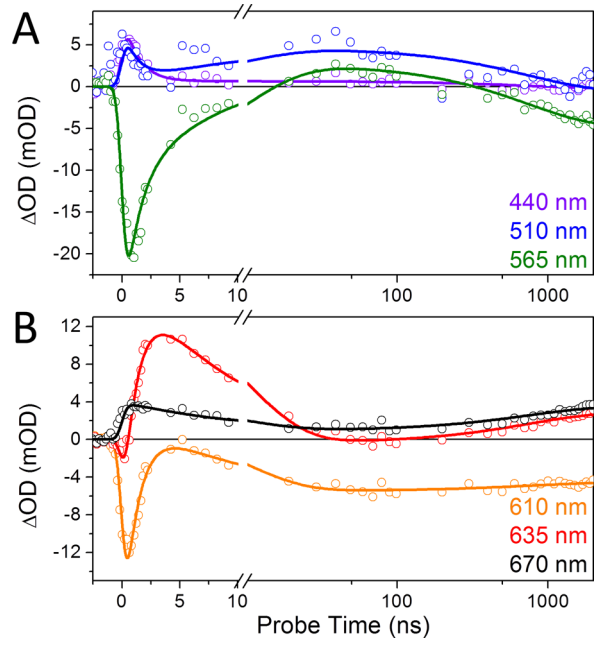

Figure 7. Secondary (<1 μs) kinetics of the reverse reaction ($P_o \rightarrow P_v$) at specific wavelengths as indicated in the legend in the (A) blue and (B) red regions of the probe range. Data (open circles) are shown with global fits (lines) described by the model shown in Figure 12.

intermediate qualitatively resembles Lumi-O_r (Figure 6A, black curve), but its spectrum is broader and more red-shifted. Meta-O_r persists to 100 μs with no apparent evolution (data not shown). These complex dynamics result in multiphasic traces (Figure 7) that were well-described by the sequential global analysis model discussed below (solid curves). At 610 nm (Figure 7B), both GSB evolution and the progress of overlapping photoproduct intermediates are detected. ESA decay is tracked at 440 and 510 nm (Figure 7A). Growth and decay of the Meta-O_g intermediate are clearly resolved at 565 nm (Figure 7A), whereas the decay of the Lumi-O_r population and growth of Meta-O_r can be resolved at 635 and 670 nm (Figure 7B).

One Millisecond Spectra. Individual 1 ms spectra were extracted from the ultrafast data by measuring TA signals before the pump pulse (i.e., the pre-time-zero signals[20]). In Figure 8, the 1 ms spectra (red curves) for both directions are

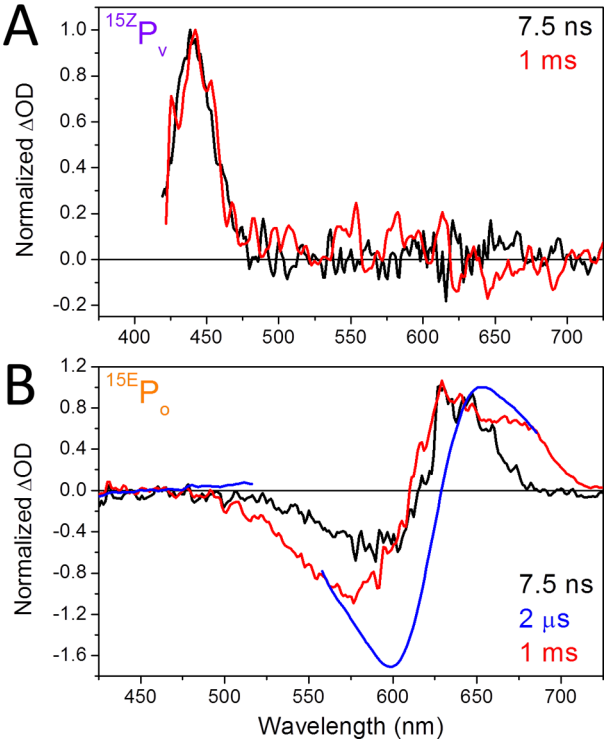

Figure 8. Scaled 1 ms transient spectra (red curves) compared to the 7.5 ns spectra (black curves) collected in the ultrafast experiments for the (A) forward and (B) reverse reactions. Scaled 2 μs spectrum (blue curve) is also shown for the (B) reverse reaction. Spectra are normalized at peak absorption wavelengths.

overlaid with the corresponding 7.5 ns spectra from the ultrafast data set. For the forward reaction (Figure 8A), the 7.5 ns and 1 ms spectra are remarkably similar, which indicates little to no spectral evolution occurs between 7.5 ns and 1 ms. This result is consistent with the similar lack of evolution in secondary signals (Figure 4).

For the reverse reaction, the 1 ms and 7.5 ns spectra are similar but not identical (Figure 8B). There is a slight broadening of the red edge of the absorption band (630–660 nm) at 1 ms. We observe a clear difference between the 2 μs and 1 ms spectra: there is additional absorption from 635 to 640 nm at 1 ms that is not observed at 2 μs. This resembles a longer-living Lumi-O_r subpopulation that is not observed in the secondary signals (Figure 6B). The difference is likely ascribed to the differing excitation conditions used in the primary (565 nm) and secondary (532 nm) experiments, in keeping with the apparent wavelength dependence of excited-state lifetime noted above. Similar excitation-wavelength dependence in the reverse reaction photodynamics was reported for the red/green CBCR NpR6012g4.[27,34]

dx.doi.org/10.1021/bi4015538 | *Biochemistry* 2014, 53, 1029–1040

Table 1. Forward, $P_v \rightarrow P_o$, Global Analysis Parameters

	ESI1 (58%)	ESI2 (29%)	ESI3 (13%)	Lumi-V_b
$\tau_{effective}$	0.7 ps	5.8 ps	82 ps	14 ns
τ	2 ps (Lumi-V_b)	180 ps (Lumi-V_b)	82 ps (P_v GS)	14 ns
	1.1 ps (P_v GS)	6 ps (P_v GS)		
branching yield	36% (Lumi-V_b)	3% (Lumi-V_b)	0% (Lumi-V_b)	
	64% (P_v GS)	97% (P_v GS)	100% (P_v GS)	

GLOBAL ANALYSIS

All four data sets were analyzed with global analysis techniques that fit the data to multicomponent models in which populations coevolve in time with time-independent spectra.[35,36] The goal of this analysis is to dissect the measured data into the evolution of constituent populations; more details of the application of this analysis to other CBCRs are presented elsewhere.[20,26−28] If the postulated target model correctly represents the underlying photodynamics of the sample, then the extracted time-independent spectra are species-associated difference spectra (SADS) and represent the true difference spectra for the constituent populations. If the model is incorrect, then the extracted spectra are evolution-associated difference spectra (EADS) and are superpositions of SADS. Prior to constructing the target model, each data set was analyzed with a sequential model (Supporting Information) to generate unbiased sequential EADS with increasing lifetimes (Figures S2−S5). Although the sequential EADS do not normally represent the correct spectra of the constituent species, this approach is useful in estimating the number of distinct kinetic species and their apparent lifetimes. However, a simple spectral analysis based on the sequential EADS analysis provides valuable a priori information in constructing a viable target model.[26,27] Secondary photodynamics were not analyzed past the sequential EADS approach because we observed no clear features of inhomogeneous or branched dynamics, such as multiexponential decay kinetics with no spectral evolution. All target models presented here exhibit excellent fits to the data (Figures 3−5 and 7, solid curves).

Primary Forward Photodynamics ($^{15Z}P_v \rightarrow {}^{15E}$Lumi-$V_b$). The sequential EADS analysis of the forward primary signals (Figure S2) showed that the data can be separated into the superposition of two unique spectra ($^{15Z}P_v$* and ^{15E}Lumi-V_b) evolving on four resolvable time scales (Figures S2 and S3). Multiexponential decay kinetics of $^{15Z}P_v$* were interpreted as arising from inhomogeneous subpopulations, as observed for other CBCRs.[20,26−28] The three excited-state $^{15Z}P_v$* populations (ESI1−ESI3) decay with 700 fs, 5.8 ps, and 82 ps time scales into the primary photoproduct, ^{15E}Lumi-V_b, which then decays on a 14 ns time scale (Table 1 and Figure S2B). These results, together with the difference between the sequential EADS (Figure S2C), allowed us to construct the target model shown in Figure 9A. In this target model, we postulate a heterogeneous $^{15Z}P_V$ dark state as the source of three $^{15Z}P_V$* subpopulations, with two producing ^{15E}Lumi-V_b. The relative occupancies of the $^{15Z}P_V$ subpopulations were estimated to be 58:29:13 on the basis of the assumption that the three $^{15Z}P_v$* SADS (ESI 1−ESI3 from Figure 9A) exhibit comparable amplitudes and spectra.[26,27] Only the two faster ESI1 and ESI2 populations generate ^{15E}Lumi-V_b, as suggested from sequential EADS analysis (Figure S2C), and both have similar spectra. The unproductive ESI3 is spectrally distinct from the others, with a weaker red ESA band (Figure 9B); its relative occupancy is thus somewhat uncertain.

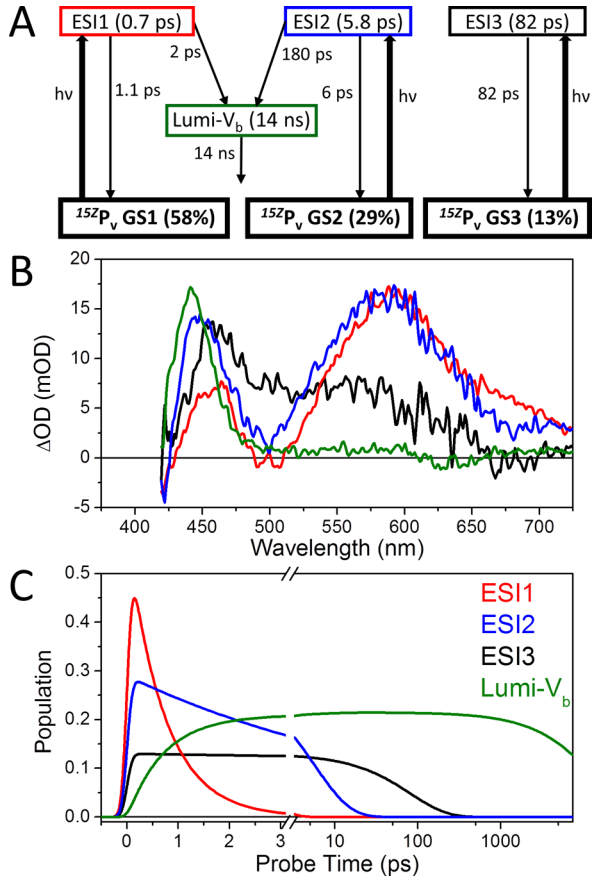

Figure 9. Target analysis ultrafast (<8 ns) forward ($P_v \rightarrow P_o$) reaction signals after 400 nm excitation. (A) Target model describing the spectral components and the corresponding time constants. (B) SADS of the target model in panel A. (C) Concentration versus time profile of each spectral species according to the target model in panel A.

The quantum yield, Φ, of generating the primary ^{15E}Lumi-V_b photoproduct was fixed to 21% within the target model (Figure 9). Our previous TA studies of CBCRs and phytochromes have used independent estimates of quantum yield for the same protein,[37] have used spectrally similar proteins of known quantum yield as references,[28] or have used more sophisticated pump−dump-probe techniques to measure quantum yield more explicitly.[25] Unfortunately, NpF2164g3, as the first insert-Cys CBCR with characterized primary dynamics, does not have a good reference sample with known Φ. We therefore take an indirect approach to estimate Φ for NpF2164g3. To date, we have characterized 16 CBCRs using ultrafast TA spectroscopy[20,26−28] (and unpublished data). Overall, we find that the amplitude of the primary photoproduct as estimated from the SADS obtained in global analysis is comparable to the amplitude of the red-most ESA band. Although this is an arbitrary feature, it is observed in all transient studies of CBCR to date. We therefore assumed it to be valid for the

dx.doi.org/10.1021/bi4015538 | Biochemistry 2014, 53, 1029−1040

photodynamics of NpF2164g3. On the basis of this assumption, we varied Φ for the forward reaction until the SADS amplitudes of ^{15E}Lumi-V_b and ESI populations were of comparable amplitudes (Figure 9B), giving the value of 21% used in the final target model. The same approach is used to estimate Φ for the reverse reaction described below.

Secondary Forward Photodynamics (^{15Z}Lumi-V_b → $^{15E}P_o$). Sequential EADS analysis of the secondary (>10 ns to 100 μs) forward dynamics is displayed in Figure 10. Although

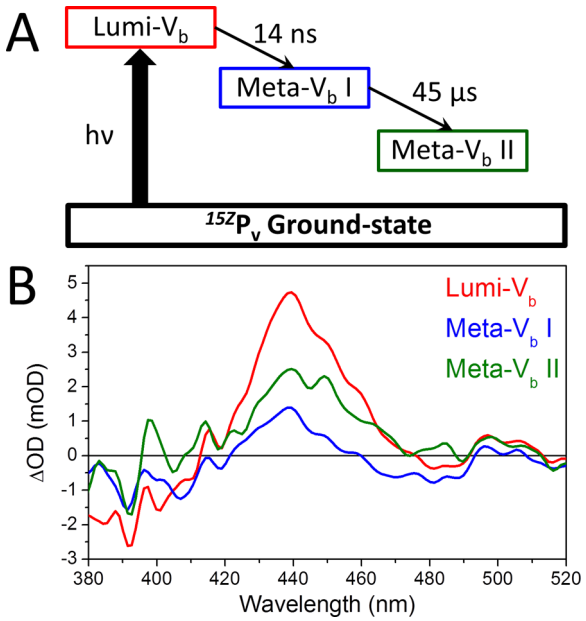

Figure 10. Sequential EADS analysis of the secondary forward ($^{15Z}P_v$ → $^{15E}P_o$) reaction kinetics in Figure 4. (A) Sequential model describing the dynamics. (B) EADS of the sequential model in panel A.

these data are arguably very noisy, the global analysis is capable of extracting underlying dynamics, especially with small spectral changes as discussed below. The initial decay of Lumi-V_b observed in the ultrafast data (14 ns, Figure 9C) is clearly resolved, and as expected, on the basis of the raw data (Figure 4B), there is a subsequent growth in the same region (Figure 10B). No red-shifted intermediate population was observed, indicating that adduct dissociation occurs on a >1 ms time scale. This result is corroborated by the 1 ms spectrum from the ultrafast data (Figure 8A). In the sequential model (^{15E}Lumi-V_b, → Meta-V_b I → Meta-V_b II), the ^{15E}Lumi-V_b evolves into Meta-V_b I with no clear spectral shifting, albeit with a decreased amplitude that increases slightly as Meta-V_b I evolves into Meta-V_b II. The three populations exhibit little to no spectral difference from each other, although the change in absorption amplitude between them suggests a shift in extinction coefficient. The final state observed, Meta-V_b II, has a peak absorption at approximately 440 nm (Figure 10B). This is comparable to the stable blue-absorbing photoproduct of the insert-Cys CBCR NpR1597g2 (448 nm[6]) and is distinct from the primary photoproduct formed by the DXCF CBCR Tlr0924, which absorbs at shorter wavelengths.[20]

Primary Reverse Photodynamics ($^{15E}P_o$ → ^{15Z}Lumi-O_r). As with the forward reaction, photoexcitation of the orange-absorbing $^{15E}P_o$ photoproduct generates multiphasic excited-state decay kinetics, with lifetimes of 4.25, 20, and 460 ps

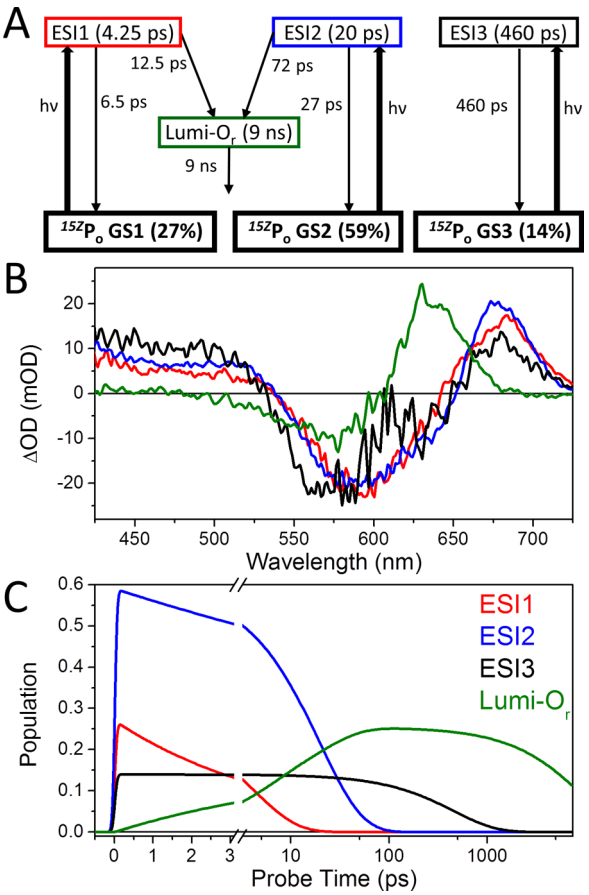

Figure 11. Target analysis of the ultrafast reverse ($^{15E}P_o$ → $^{15Z}P_v$) reaction kinetics. (A) Target model describing the evolving species with corresponding time constants. (B) SADS of the target model in panel A. (C) Concentration profiles for each species according to the target model in panel A.

(Figure 11A and Table 2). Sequential EADS analysis decomposed the TA signals into two separate spectra, $^{15E}P_o$* and ^{15Z}Lumi-O_r, evolving with differing dynamics (Figure S4). Sequential EADS analysis also indicated that only the two faster ESI1 and ESI2 populations generate ^{15E}Lumi-O_r (Figures 11A and S6). We constructed a target model similar to that of the forward reaction, with different ESI arising because of ground-state heterogeneity rather than bifurcation on the excited-state surface (Figure 11A). Relative occupancies of the three coexisting excited-state populations were estimated at 27:59:14 to satisfy the assumption that the three $^{15E}P_o$* SADS are comparable in shape and amplitude (Figure 11B). As for the forward reaction, we estimated Φ by tuning the branching ratios associated with the productive ESI species to produce amplitude agreement between the excited-state and photoproduct SADS. This method yielded an estimated Lumi-O_r Φ of ∼26% (Figure 11C and Table 2).

Secondary Reverse Photodynamics (^{15Z}Lumi-O_r → $^{15Z}P_v$). The secondary signals for the reverse reaction were well-described by a four-component sequential EADS analysis (Figures 7 and 12). The initial EADS1 (Figure 12B) is attributed to the excited-state P_o* populations, and EADS2 (blue curve) is ascribed to Lumi-O_r observed in the ultrafast data (Figure 11B). This Lumi-O_r population decays with a 9 ns

dx.doi.org/10.1021/bi4015538 | Biochemistry 2014, 53, 1029−1040

Table 2. Reverse, $P_o \rightarrow P_v$, Global Analysis Parameters

	ESI1 (27%)	ESI2 (59%)	ESI3 (14%)	Lumi-O_r
$\tau_{effective}$	4.25 ps	20 ps	460 ps	9 ns
τ	12.5 ps (Lumi-O_r)	72 ps (Lumi-O_r)	460 ps (P_o GS)	9 ns
	6.5 ps (P_o GS)	27 ps (P_o GS)		
branching yield	34% (Lumi-O_r)	27% (Lumi-O_r)	0% (Lumi-O_r)	
	66% (P_o GS)	73% (P_o GS)	100% (P_o GS)	

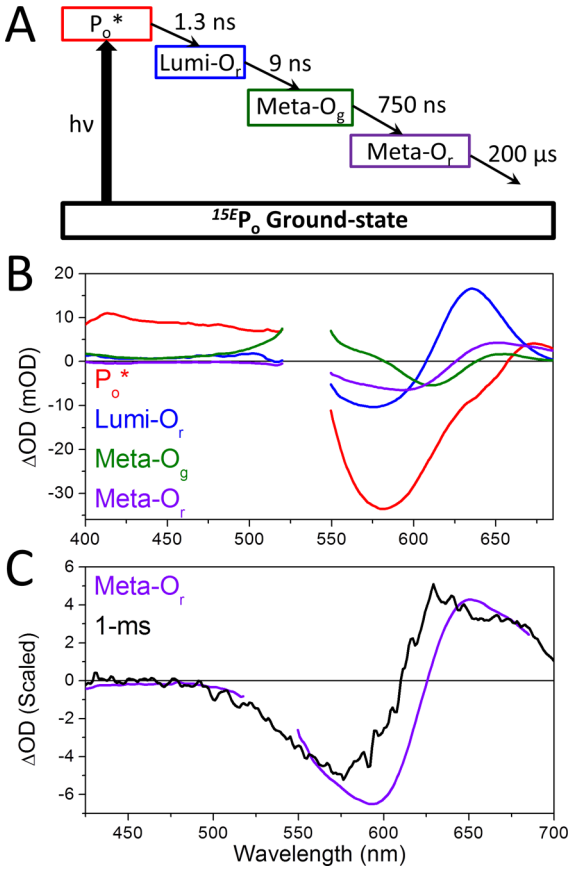

Figure 12. Sequential EADS analysis of the long time reverse ($^{15E}P_o \rightarrow {}^{15Z}P_v$) reaction kinetics in Figures 6 and 7. (A) Sequential model describing the dynamics. (B) EADS of the sequential model in panel A. (C) Comparison of the final Meta-O_r population with the 1 ms spectrum from the ultrafast data set. There exists a ~25 nm discrepancy in the maximum absorption wavelengths between the two spectra, indicating a red shift of the Meta-O_r between 2 μs and 1 ms.

lifetime, which is consistent with the 9 ns decay observed in the ultrafast data (Figure 11). However, the excited-state P_o* decay observed in the secondary dynamics (1.3 ns) is significantly slower that the longest lifetime of the primary data (460 ps, Figure 11A). This discrepancy is likely due to the excitation wavelength dependence on the excited-state dynamics (565 vs 532 nm pulses for ultrafast and secondary dynamics, respectively, from Figure S1) and is discussed further below.

EADS3 (Figure 12B) peaks near 520 nm and is ascribed to a blue-shifted Meta-O_g photoproduct that decays on a 750 ns time scale. The 9 ns rise of Meta-O_g explains the apparent decay of the bleach band observed in the ultrafast data (Figure 5C). EADS4 (Figure 12B) is qualitatively similar to Lumi-O_r (or EADS2) but is red-shifted by ~20 nm and appears at later times; therefore, it is attributed to Meta-O_r. Comparison of the ^{15Z}Meta-O_r spectrum (EADS4) to the 1 ms ultrafast spectrum (Figure 12C) reveals a good agreement in the red-edge region; however, the 1 ms spectrum shows an extra blue-edge absorption that strongly resembles the ^{15Z}Lumi-O_r population with a peak at ~640 nm (Figure 8B). This discrepancy is thought to originate from differing excitation wavelengths of the two data sets (see below).

The secondary reverse-reaction dynamics of NpF2164g3 are thus complex. The red-shifted ^{15Z}Lumi-O_r primary photoproduct initially blue shifts to generate ^{15Z}Meta-O_g, which then red shifts to generate ^{15Z}Meta-O_r. Such alternating spectral shifts have not been reported in the secondary dynamics of the red/green CBCRs AnPixJg2[30] and NpR6012g4.[31] Completion of the reverse reaction in NpF2164g3 requires formation of the C10−Cys adduct with PCB to produce the blue-shifted $^{15Z}P_v$ state. The absence of a blue-shifted intermediate at 1 ms after excitation of $^{15E}P_o$ (Figure 8) indicates that adduct formation is a slower process (>1 ms).

DISCUSSION

We report transient dynamics on both primary (<10 ns) and secondary (10 ns to 1 ms) time scales for both reaction directions in the violet/orange insert-Cys CBCR NpF2164g3. As with all other CBCRs to date, we interpret the observed multiphasic excited-state decay in terms of ground-state heterogeneity. On these time scales, we did not resolve formation or elimination of the second linkage, which is also slow in the DXCF CBCR Tlr0924.[20] We were able to construct a simplified scheme for the NpF2164g3 photocycle from the four data sets presented (Figure 13A), omitting the postulated ground-state heterogeneity (Figures 9A and 11A) for clarity. Compared to previous studies,[27,34,37] this work allows us to examine possible excitation-wavelength dependence while also providing a detailed comparison to similar work on the DXCF CBCR Tlr0924,[20] a member of the other CBCR subfamily that employs two-Cys photocycles.[6]

Effects of the excitation wavelength on photoreceptor dynamics are ubiquitous in the study of CBCRs. The green-absorbing states of both NpR6012g4 and RcaE exhibit wavelength-dependent effects on the GSB peak absorption and line shape;[27,34] the fact that such effects are present in the raw data rules out the possibility that these effects are artifacts introduced during global analysis. Recent studies attribute such effects to unequal excitation of heterogeneous ground-state subpopulations by different excitation pulses.[27,34]

For NpF2164g3, we initiated reverse primary and secondary reaction signals with different pulses. In the forward reaction, the secondary signals generated by 355 nm pulses are not of sufficient quality for comparison with the primary signals generated by 400 nm excitation (in part because of the rapid photodegradation of the sample). For the reverse reaction, the primary and secondary dynamics were initiated by 565 and 532 nm pulses, respectively (Figure S1). The primary reverse reaction spectra (Figure 5A) exhibit an ESA band from 425 to

dx.doi.org/10.1021/bi4015538 | Biochemistry 2014, 53, 1029−1040

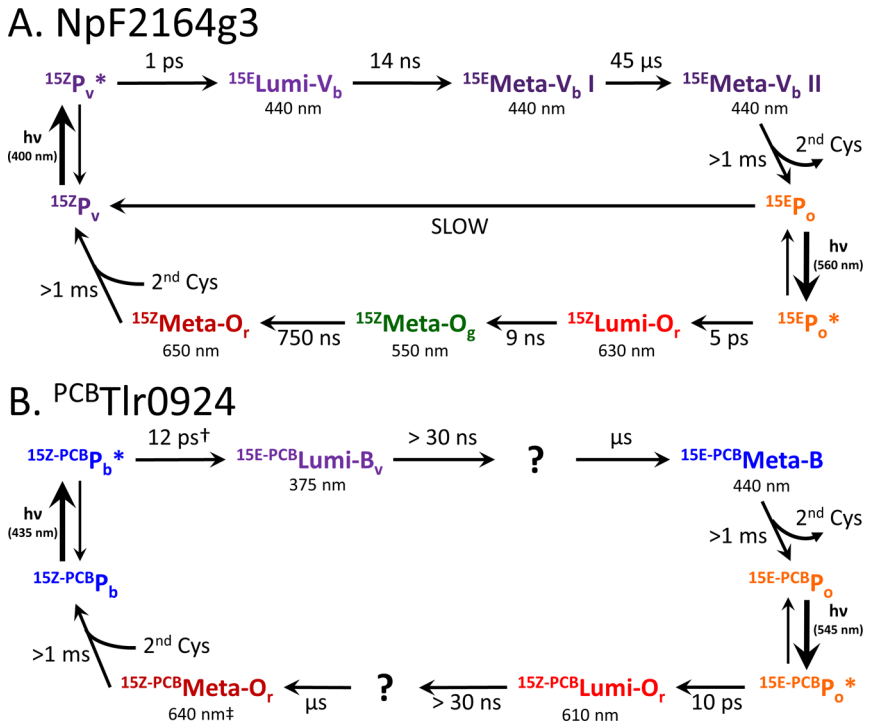

Figure 13. Forward and reverse photocycles for the violet/orange NpF2164g3 photocycle compared with those of ^{PCB}Tlr0924. (A) Adduct formation to the PCB chromophore occurs between ^{15E}Meta-O_r and $^{15E}P_o$ in the forward direction and bond cleavage occurs between Meta-O_r and P_v in the reverse direction on >1 ms time scales. (B) Secondary dynamics were not collected for Tlr0924, so not all species are resolved.[20] The excited-state lifetimes are multiphasic and only the fastest phase is indicated. †PCB and PVB sample. ‡IAM trapped spectrum.

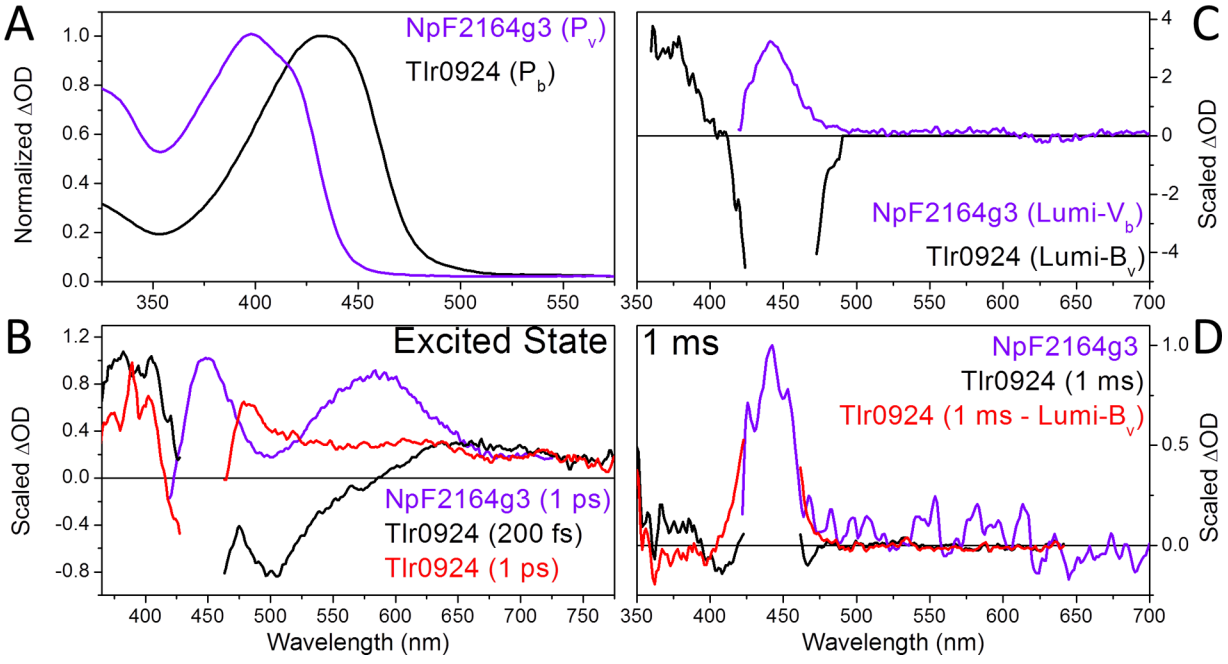

Figure 14. Comparison of forward (*15Z* → *15E*) conversions of NpF2164g3 (solid purple curves) and Tlr0924 (dashed red and black curves). (A) Ground-state absorption spectra of the dark-adapted states normalized at the peak absorption wavelengths. (B) One picosecond excited-state spectrum of NpF2164g3 (purple curve) normalized with the 100 fs spectrum of Tlr0924 (black dashed curve) at the peaks of the ESA bands. (C) Primary Lumi-V_b photoproduct spectra for each sample scaled at the wavelengths of maximum absorbance. (D) One millisecond spectrum for NpF2164g3 compared to that of Tlr0924 (black curve). The difference between Tlr0924's 1 ms and Lumi-V_b spectra is shown in red to illustrate the area of absorbance in the 1 ms spectrum.[20]

525 nm that decays completely by 6.6 ns, whereas the secondary signals exhibit a long-lived ESA (Figures 6 and 12A). In addition, the two data sets exhibit distinct features in the GSB: primary data show a negative GSB from 550 to 625 nm, whereas secondary data show a large positive band in the same region (Figures 5A and 6). The source of this difference in the

dx.doi.org/10.1021/bi4015538 | *Biochemistry* 2014, 53, 1029−1040

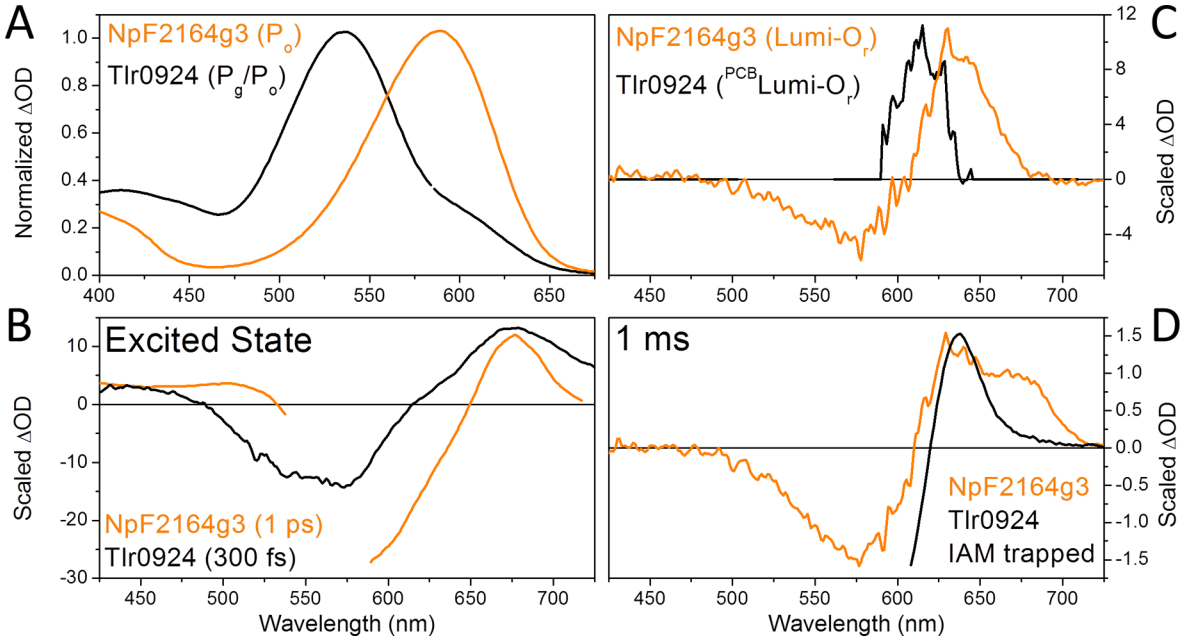

Figure 15. Comparison of reverse (*15E* → *15Z*) conversions of NpF2164g3 (orange curves) and ^{PCB}Tlr0924 (dashed curves) domains. (A) Ground-state absorption spectra of the metastable *15E* states normalized to the peak absorption wavelengths. The PVB absorbance at 540 nm is clearly separated from the PCB absorbance at 600 nm in ^{PCB}Tlr0924. (B) One picosecond excited-state spectrum of NpF2164g3 (orange curve) scaled with the 300 fs spectrum of ^{PCB}Tlr0924 (black dashed curve). (C) Primary ^{PCB}Lumi-O$_r$ photoproduct spectra for each sample scaled at the wavelengths of maximum absorbance (the PVB photoproduct is not shown). (D) One millisecond spectrum for NpF2164g3 scaled to that of the IAM trapped ^{PCB}Tlr0924 (black dashed curve).[20]

GSB is unknown, but it is unlikely to have been caused by scattered excitation light in the secondary pulse because it is quite narrow spectrally. Therefore, higher-energy excitation of *15E* NpF2164g3 initiated longer-living excited-state dynamics than lower-energy excitation. This trend is opposite to that observed in NpR6012g4.[27]

Both NpF2164g3 and Tlr0924 utilize two-Cys photocycles, but they are in different subfamilies and contain different second Cys residues.[6] Although Tlr0924 contains both PCB and PVB populations, it has been possible to decompose parallel photocycles for the two chromophore populations.[9,20] Secondary dynamics have not yet been reported for Tlr0924, but comparative analysis of 1 ms signals with spectra obtained from chemical modification studies[12] allowed construction of a simplified scheme for the PCB population similar to that derived in this work for NpF2164g3.[20] In Figure 13B, we present the Tlr0924 scheme using the nomenclature system employed in the current work to provide direct comparison to NpF2164g3, with the caveat that the absence of data on secondary dynamics precludes identification of intermediates formed between the nanosecond and millisecond time scales. Figures 14 and 15 contrast the equivalent spectra for individual species in the two proteins for the forward and reverse reactions, respectively.

The forward reactions exhibit surprising differences. The ground-state spectrum of *15Z* NpF2164g3 is blue-shifted relative to that of Tlr0924 (Figure 14A) and forms the primary photoproduct more rapidly (1 vs 12 ps, Figure 13) despite broadly similar excited-state features (Figure 14B). Interestingly, these two proteins also give rise to distinctly different primary photoproducts: the ^{15E}Lumi-V$_b$ product formed by NpF2164g3 is red-shifted relative to the ground state, as is typical for CBCRs,[26−28,30] but the ^{15E}Lumi-B$_v$ product of Tlr0924 is blue-shifted relative to the ground state and the NpF2164g3 primary photoproduct (Figure 14C). This suggests that the B−C ring system of the ^{15Z}P$_v$ state of Np2164g3 is constrained to a smaller space (i.e., twisted), which relaxes after photoisomerization. That of Tlr0924 is more stretched out as ^{15Z}P$_b$ (i.e., splayed about the C15 region), yet it may be more constrained by methyl−methyl group clashes or protein−chromophore steric clashes after photoisomerization. The secondary photodynamics are more similar, with ^{15E}Lumi-B$_v$ in Tlr0924 evolving by 1 ms to yield a ^{15E}Meta-B$_b$ intermediate similar to ^{15E}Meta-V$_2$ in NpF2164g3 (Figure 14D). This species persists past 1 ms in both proteins and is similar to the stable blue-absorbing photoproduct of the insert-Cys CBCR NpR1597g2.[6] We therefore propose that it is the last species before adduct elimination.

The explanation for these differences may lie in the differences between the two subfamilies. In NpF2164g3, the second linkage may be associated with a large, unstructured loop,[23] which is not the case in DXCF CBCRs.[22] This extra flexibility could explain the differences in the forward photoreaction because the bilin-binding pocket of NpF2164g3 would be less rigid, allowing more chromophore relaxation during formation of the primary photoproduct. Thus, Tlr0924 traps an unusual blue-shifted photoproduct that must relax on the ground-state surface to achieve a red-shifted chromophore conformation favorable for adduct elimination. By contrast, NpF2164g3 achieves such a conformation more rapidly, and ground-state evolution changes the extinction coefficient but not the peak wavelength, perhaps because of rearrangement of protein residues or of the spectrally silent propionate side chains of the bilin chromophore.

This hypothesis predicts much more similar behavior for these two proteins in the reverse reaction because the second linkage is not present. The Tlr0924 ground-state spectra are complicated by the mixture of PCB and PVB (Figure 15A),

which is not a factor for the doubly linked *15Z* states.[9] In the reverse direction, the excited-state spectra of the two CBCRs are again broadly similar (Figure 15B). Both NpF2164g3 and the PCB population in Tlr0924 yield spectrally similar Lumi-O_r photoproducts (Figure 15C) with comparable kinetics (5 vs 10 ps, Figure 13). Subsequent evolution also leads to accumulation of similar states prior to adduct formation (Figure 15D) if one compares the 1 ms NpF2164g3 spectrum to that obtained for Tlr0924 by chemical trapping.[12] Interestingly, a prominent red-edge shoulder in NpF2164g3 is absent in Tlr0924. It is not yet clear whether this reflects differences between the proteins or between the experimental methodologies, but the red-edge shoulder was also observed in NpF2164g3 under static conditions if the second Cys residue was inactivated through chemical trapping or site-directed mutagenesis.[6] Overall, this analysis demonstrates that the reverse reaction is indeed more similar for these two CBCRs than the forward reaction.

We therefore propose that the reverse photocycles of orange-absorbing ^{15E}CBCRs will be broadly similar, exhibiting a red-shifted primary photoproduct on a picosecond time scale. By contrast, the photocycles of doubly linked photostates are clearly more diverse. Current data are consistent with the hypothesis that these differences arise among different CBCR subfamilies because of the flexibility or rigidity of the pocket, a hypothesis that will require further testing. Fortunately, the ever-increasing number of characterized CBCRs provides ample opportunity for such analyses. For example, in addition to insert-Cys CBCRs such as NpF2164g3 with labile second linkages, there are also insert-Cys CBCRs with stable second linkages that yield blue-absorbing photoproducts. Such photocycles could arise because of more rigid insert-Cys chromophore-binding pockets and hence could behave more like Tlr0924. There are also DXCF CBCRs with reversed green/blue photocycles.[9,38] The work presented here establishes the basis to examine more CBCRs within the framework of a structurally based, experimentally testable hypothesis, an approach that should permit improvements in our understanding of chromophore dynamics and protein−chromophore interactions in the diverse array of CBCR photocycles.

■ ASSOCIATED CONTENT

Supporting Information

Nomenclature, absorption spectra with all four excitation wavelengths, sequential analysis of the NpF2164g3 forward reaction, kinetic traces of forward reaction dynamics, sequential analysis of the NpF2164g3 reverse reaction, reverse reaction traces of reverse reaction dynamics, and reverse reaction EADS analysis differences. This material is available free of charge via the Internet at http://pubs.acs.org.

■ AUTHOR INFORMATION

Corresponding Author

*Tel.: (530) 754-9075; E-mail: dlarsen@ucdavis.edu.

Author Contributions

§These authors contributed equally to this work.

Funding

This work was supported by grants from the Chemical Sciences, Geosciences, and Biosciences Division, Office of Basic Energy Sciences, Office of Science, United States Department of Energy (DOE DE-FG02-09ER16117) to J.C.L. and D.S.L.

Notes

The authors declare no competing financial interest.

■ ACKNOWLEDGMENTS

Dr. Mikas Vengris (Light Conversion Ltd.) is acknowledged for the donation of the global and target analysis software package.

■ REFERENCES

(1) Butler, W. L., Norris, K. H., Siegelman, H. W., and Hendricks, S. B. (1959) Detection, assay, and preliminary purification of the pigment controlling photoresponsive development of plants. *Proc. Natl. Acad. Sci. U.S.A. 45*, 1703−1708.

(2) Hughes, J. (2010) Phytochrome three-dimensional structures and functions. *Biochem. Soc. Trans. 38*, 710−716.

(3) Rockwell, N. C., and Lagarias, J. C. (2010) A brief history of phytochromes. *ChemPhysChem 11*, 1172−1180.

(4) Auldridge, M. E., and Forest, K. T. (2011) Bacterial phytochromes: More than meets the light. *Crit. Rev. Biochem. Mol. Biol. 46*, 67−88.

(5) Kim, P. W., Rockwell, N. C., Freer, L. H., Chang, C.-W., Martin, S. S., Lagarias, J. C., and Larsen, D. S. (2013) Unraveling the primary isomerization dynamics in cyanobacterial phytochrome Cph1 with multipulse manipulations. *J. Phys. Chem. Lett. 4*, 2605−2609.

(6) Rockwell, N. C., Martin, S. S., Feoktistova, K., and Lagarias, J. C. (2011) Diverse two-cysteine photocycles in phytochromes and cyanobacteriochromes. *Proc. Natl. Acad. Sci. U.S.A. 108*, 11854−11859.

(7) Ikeuchi, M., and Ishizuka, T. (2008) Cyanobacteriochromes: A new superfamily of tetrapyrrole-binding photoreceptors in cyanobacteria. *Photochem. Photobiol. Sci. 7*, 1159−1167.

(8) Enomoto, G., Hirose, Y., Narikawa, R., and Ikeuchi, M. (2012) Thiol-based photocycle of the blue and teal light-sensing cyanobacteriochrome Tlr1999. *Biochemistry 51*, 3050−3058.

(9) Rockwell, N. C., Martin, S. S., Gulevich, A. G., and Lagarias, J. C. (2012) Phycoviolobilin formation and spectral tuning in the DXCF cyanobacteriochrome subfamily. *Biochemistry 51*, 1449−1463.

(10) Rockwell, N. C., Njuguna, S. L., Roberts, L., Castillo, E., Parson, V. L., Dwojak, S., Lagarias, J. C., and Spiller, S. C. (2008) A second conserved GAF domain cysteine is required for the blue/green photoreversibility of cyanobacteriochrome Tlr0924 from *Thermosynechococcus elongatus*. *Biochemistry 47*, 7304−7316.

(11) Rockwell, N. C., Martin, S. S., and Lagarias, J. C. (2012) Red/green cyanobacteriochromes: Sensors of color and power. *Biochemistry 51*, 9667−9677.

(12) Rockwell, N. C., Martin, S. S., and Lagarias, J. C. (2012) Mechanistic insight into the photosensory versatility of DXCF cyanobacteriochromes. *Biochemistry 51*, 3576−3585.

(13) Ishizuka, T., Kamiya, A., Suzuki, H., Narikawa, R., Noguchi, T., Kohchi, T., Inomata, K., and Ikeuchi, M. (2011) The cyanobacteriochrome, TePixJ, isomerizes its own chromophore by converting phycocyanobilin to phycoviolobilin. *Biochemistry 50*, 953−961.

(14) Ulijasz, A. T., Cornilescu, G., von Stetten, D., Cornilescu, C., Escobar, F. V., Zhang, J. R., Stankey, R. J., Rivera, M., Hildebrandt, P., and Vierstra, R. D. (2009) Cyanochromes are blue/green light photoreversible photoreceptors defined by a stable double cysteine linkage to a phycoviolobilin-type chromophore. *J. Biol. Chem. 284*, 29757−29772.

(15) Ma, Q., Hua, H. H., Chen, Y., Liu, B. B., Kramer, A. L., Scheer, H., Zhao, K. H., and Zhou, M. (2012) A rising tide of blue-absorbing biliprotein photoreceptors: Characterization of seven such bilin-binding GAF domains in *Nostoc* sp. PCC7120. *FEBS J. 279*, 4095−4108.

(16) Ishizuka, T., Narikawa, R., Kohchi, T., Katayama, M., and Ikeuchi, M. (2007) Cyanobacteriochrome TePixJ of *Thermosynechococcus elongatus* harbors phycoviolobilin as a chromophore. *Plant Cell Physiol. 48*, 1385−1390.

(17) Song, J. Y., Cho, H. S., Cho, J. I., Jeon, J. S., Lagarias, J. C., and Park, Y. I. (2011) Near-UV cyanobacteriochrome signaling system

elicits negative phototaxis in the cyanobacterium *Synechocystis* sp. PCC 6803. *Proc. Natl. Acad. Sci. U.S.A. 108*, 10780−10785.
(18) Narikawa, R., Suzuki, F., Yoshihara, S., Higashi, S.-i., Watanabe, M., and Ikeuchi, M. (2011) Novel photosensory two-component system (PixA-NixB-NixC) involved in the regulation of positive and negative phototaxis of cyanobacterium *Synechocystis* sp. PCC 6803. *Plant Cell Physiol. 52*, 2214−2224.
(19) Yoshihara, S., Katayama, M., Geng, X. X., and Ikeuchi, M. (2004) Cyanobacterial phytochrome-like PixJ1 holoprotein shows novel reversible photoconversion between blue- and green-absorbing forms. *Plant Cell Physiol. 45*, 1729−1737.
(20) Freer, L. H., Kim, P. W., Corley, S. C., Rockwell, N. C., Zhao, L., Thibert, A. J., Lagarias, J. C., and Larsen, D. S. (2012) Chemical inhomogeneity in the ultrafast dynamics of the DXCF cyanobacteriochrome Tlr0924. *J. Phys. Chem. B 116*, 10571−10581.
(21) Narikawa, R., Ishizuka, T., Muraki, N., Shiba, T., Kurisu, G., and Ikeuchi, M. (2013) Structures of cyanobacteriochromes from phototaxis regulators AnPixJ and TePixJ reveal general and specific photoconversion mechanism. *Proc. Natl. Acad. Sci. U.S.A. 110*, 918−923.
(22) Burgie, E. S., Walker, J. M., Phillips, G. N., Jr., and Vierstra, R. D. (2013) a photo-labile thioether linkage to phycoviolobilin provides the foundation for the blue/green photocycles in DXCF-cCyanobacteriochromes. *Structure 21*, 88−97.
(23) Lim, S., Rockwell, N. C., Martin, S. S., Lagarias, J. C., and Ames, J. B. (2013) H, N, and C chemical shift assignments of cyanobacteriochrome NpF2164g3 in the photoproduct state. *Biomol. NMR Assignments* [Online early access], DOI: 10.1007/s12104-013-9496-0, Published Online: June 9, 2013.
(24) Ishizuka, T., Shimada, T., Okajima, K., Yoshihara, S., Ochiai, Y., Katayama, M., and Ikeuchi, M. (2006) Characterization of cyanobacteriochrome TePixJ from a thermophilic cyanobacterium *Thermosynechococcus elongatus* strain BP-1. *Plant Cell Physiol. 47*, 1251−1261.
(25) Kim, P. W., Freer, L. H., Rockwell, N. C., Martin, S. S., Lagarias, J. C., and Larsen, D. S. (2012) Second-chance forward isomerization dynamics of the red/green cyanobacteriochrome NpR6012g4 from *Nostoc punctiforme*. *J. Am. Chem. Soc. 134*, 130−133.
(26) Kim, P. W., Freer, L. H., Rockwell, N. C., Martin, S. S., Lagarias, J. C., and Larsen, D. S. (2012) Femtosecond photodynamics of the red/green cyanobacteriochrome NpR6012g4 from *Nostoc punctiforme*. 1. Forward dynamics. *Biochemistry 51*, 608−618.
(27) Kim, P. W., Freer, L. H., Rockwell, N. C., Martin, S. S., Lagarias, J. C., and Larsen, D. S. (2012) Femtosecond photodynamics of the red/green cyanobacteriochrome NpR6012g4 from *Nostoc punctiforme*. 2. Reverse dynamics. *Biochemistry 51*, 619−630.
(28) Chang, C.-W., Gottlieb, S. M., Kim, P. W., Rockwell, N. C., Lagarias, J. C. L., and Larsen, D. S. (2013) Reactive ground-state pathways are not ubiquitous in red/green cyanobacteriochromes. *J. Phys. Chem. B 117*, 11229−11238.
(29) Narikawa, R., Ishizuka, T., Ochiai, Y., Katayama, M., Kohchi, T., and Ikeuchi, M. (2007) Novel green-red photoreversible cyanobacteriochrome (AnPixJ): Is the chromophore of green-absorbing form identical to that of Pfr of phytochrome? *Plant Cell Physiol. 48*, S102−S102.
(30) Fukushima, Y., Iwaki, M., Narikawa, R., Ikeuchi, M., Tomita, Y., and Itoh, S. (2011) Photoconversion mechanism of a green/red photosensory cyanobacteriochrome AnPixJ: Time-resolved optical spectroscopy and FTIR analysis of the AnPixJ-GAF2 domain. *Biochemistry 50*, 6328−6339.
(31) Gottlieb, S. M., Corley, S. C., Madsen, D., and Larsen, D. S. (2012) A flexible light emitting diode-based broadband transient-absorption spectrometer. *Rev. Sci. Instrum.*, 83.
(32) Rockwell, N. C., Shang, L., Martin, S. S., and Lagarias, J. C. (2009) Distinct classes of red/far-red photochemistry within the phytochrome superfamily. *Proc. Natl. Acad. Sci. U.S.A. 106*, 6123−6127.
(33) Carroll, E. C., Compton, O. C., Madsen, D., Osterloh, F. E., and Larsen, D. S. (2008) Ultrafast carrier dynamics in exfoliated and functionalized calcium niobate nanosheets in water and methanol. *J. Phys. Chem. C 112*, 2394−2403.
(34) Gottlieb, S. M., Kim, P. W., Rockwell, N. C., Hirose, Y., Ikeuchi, M., Lagarias, J. C., and Larsen, D. S. (2013) Primary photodynamics of the green/red-absorbing photoswitching regulator of chromatic adaptation E domain from *Fremyella diplosiphon*. *Biochemistry 52*, 8198−8208.
(35) Holzwarth, A. R. (1996) Data analysis of time-resolved measurements, In *Biophysical Techniques in Photosynthesis* (Amesz, J., and Hoff, A. J., Eds.) pp 75−92, Kluwer Academic Publishers, Dordrecht, The Netherlands.
(36) van Stokkum, I. H. M., Larsen, D. S., and van Grondelle, R. (2004) Global and target analysis of time-resolved spectra. *Biochim. Biophys. Acta, Bioenerg. 1657*, 82−104.
(37) Kim, P. W., Rockwell, N. C., Martin, S. S., Lagarias, J. C., and Larsen, D. S. (2013) Fluoresce or not to fluoresce: Dynamic inhomogeneity in the cyanobacterial phytochrome Cph1. Submitted for publication.
(38) Bussell, A. N., and Kehoe, D. M. (2013) Control of a four-color sensing photoreceptor by a two-color sensing photoreceptor reveals complex light regulation in cyanobacteria. *Proc. Natl. Acad. Sci. U.S.A. 110*, 12834−12839.